Maria Sklodowska-Curie Actions (MSCA)
Innovative Training Networks (ITN)
H2020-MSCA-ITN-2018
Grant number 813137

Project number 813137

URBASIS-EU
New challenges for Urban Engineering Seismology

DELIVRABLE

Work Package: WP2
Number: D2.4 - Toward New Near-Field Ground Motion Prediction Equations for Induced Seismicity

Authors:	**Suroyo, Pungky**	(UoL)
Co-Authors:	Edwards, Benjamin	(UoL)

Reviewers	Bindi, Dino	(GFZ)
Approval	Management Board	
Status	Final Version	
Dissemination level	Public	
Delivery deadline	31.10.2020	
Submission date	30.10.2020	
Intranet path	https://urbasis-eu.osug.fr/Scientific-Reports-157	

D2.4: Toward New Near-Field Ground-Motion Prediction Equations for Induced Seismicity

Abstract

Induced seismicity is currently drawing public attention as a potentially significant hazard. Several studies have been conducted to develop ground-motion prediction equations (GMPEs) for induced seismicity, however, many of them still rely on the assumption that induced events have similar source and attenuation parameters to those of natural earthquakes. We use the Preston New Road (PNR), Blackpool, UK dataset recorded between 2018-2019 with local magnitudes $M_L < 3$ at distances less than 40 km to facilitate the development of GMPEs that are tuned to the key magnitude-distance range for induced seismicity applications. The study of attenuation parameters using spectral fitting methods and coda envelope decay methods is the focus of this deliverable. Using a spectral fitting method, the best overall fit is found for a frequency-independent Q model ($\alpha = 0$) with Q_s = 179.63, Q_c = 168.09, and Q_{sc} = 215.96. Whereas results from a coda envelope decay method (Q_{clt}), obtained from the four biggest events recorded at PNR, show $Q_{clt}(f) = 110(f/f_{10})^{1.04}$ between 10-25 Hz. Discrepancies in the observation of Q models can be caused by the use of different methods as well as the different signal analysis windows and focus on different wavefields. Meanwhile, the difference to the average regional Q ($Q_{Lg}(f) = 266 f^{0.53}$) is likely due to different physical rock properties sampled by locally and regionally propagating waves. Through the spectral fitting approach, the high-frequency decay parameter, κ_0, is obtained as the residual site-specific exponential decay. Observation of site condition by calculating V_{s30} using several bedrock depth assumptions and fundamental frequency (f_0) obtained from horizontal-to-vertical spectral ratios (HVSR) is also discussed in this deliverable. In addition, an updated M_L - M_W relationship model for PNR dataset is presented, which shows compatibility with the M_L - M_W model proposed by Edwards et al., (2019). A summary of preliminary observations is discussed in order to better understand ground motion attenuation and its controlling factors. These findings can subsequently be implemented for developing suitable GMPEs for induced earthquakes.

I. Introduction

Research interest in anthropogenic earthquakes or "induced" earthquakes has been significantly increased in recent years. Anthropogenic earthquakes can be generated by underground mining, artificial water reservoir impoundment, geothermal energy production, waste disposal, and hydrocarbon extraction. In spite of the fact that such events have relatively small magnitude compared to natural earthquakes, it can be a significant nuisance and in extreme conditions can lead to damage due to their close proximity to urban centres. In July and August 2014, earthquakes with magnitudes of 4.0 and 4.2 were reported near Fort St. John, British Columbia, Canada. Both were considered to have been induced by hydraulic fracturing activities (Atkinson et al., 2015). In the UK itself, the Human-Induced Earthquake Database (*HiQuake)* has noted several earthquakes that are presumed or suspected as induced seismic events, either triggered by mining, geothermal, fracking, conventional oil and gas, or construction activities (Foulger et al., 2018). The largest magnitude recorded for cases found in the UK (*HiQuake*-last updated on 9/6/2020) was 4.2 M_L in Folkestone, Kent, UK. Klose (2007) suggest that this event may have been triggered by geo-engineering of shingle accumulation in the harbour since 1806, however the evidence for this is relatively weak (Nievas et al. 2020). The most recent induced event in the UK was recorded at Preston New Road with local magnitude (M_L) 2.9 (on 2019/08/26). This event was unequivocally caused by hydraulic fracturing during shale gas exploration. Previous induced earthquakes of notable magnitude related to exploration of a shale gas exploration also occurred nearby at Preese Hall on 1 April and 27 May 2011 with magnitudes 2.3 M_L and 1.5 M_L. Both were suspected to be linked to the hydraulic fracture injections at the Preese Hall well 1 (PH1) operated by Cuadrilla Resources Ltd. (Clarke et al., 2014; de Pater and Baisch, 2011).

In order to determine the hazard of seismic activity induced by industrial activities and also develop risk mitigation, the development of ground-motion models that are well-suited for such applications is required. Since the ground motion generated by anthropogenic activities certainly has unique characteristics and different from those due to natural earthquakes, several challenges might be found, such as: (1) the focus on, and determination of, lower magnitudes than typically of interest for tectonic seismic hazard, (2) the difficulty to extrapolate directly ground-motion prediction equations (GMPEs) to those small magnitudes, (3) the regional differences in ground motion characteristics that become more apparent at smaller magnitude (e.g., Bommer et al., 2017), and (4) the variability of motion at lower earthquake magnitude is often larger due to the larger variability of stress drop compared to moderate- large events. Until recently, the prediction of ground motions for induced seismicity has been done by simply borrowing the GMPEs from nearby localities, similar tectonic environments, or by combining datasets. However, by simply 'borrowing' GMPEs for induced seismicity does not often work, and combining datasets (e.g., Douglas et al., 2013) leads to unsatisfactory variance (sigma). In order to solve this problem, it requires us to perform deconvolution of source, path/propagation, and site effects and develop the new location-specific GMPEs designed for induced seismicity (small magnitude events at close distances).

In this deliverable, we summarize analysis of ground motion prediction equations (GMPEs) for induced seismicity due to hydraulic fracturing in Preston New Road (PNR). We also discuss the efforts that have been made to observe the physical source, path, and site effects which required as a starting point to better understand the ground motion characteristics for induced seismicity and develop a new ground motion model specifically designed for the magnitude and distance range of induced seismic events.

II. Preston New Road Dataset

Types of seismicity are typically differentiated as natural or induced. Since the UK is not near a plate tectonic boundary, nor does it have any active volcanoes, the natural seismicity in the UK is low compared to more seismically active regions in the world, such as Japan, Italy, and the USA. However, induced seismicity has been a common occurrence in the UK. An effort to distinguished between natural and anthropogenic earthquakes by determining a baseline/threshold has been undertaken by Wilson et al. (2015). The study reviewed UK distribution, timing, and probable causes of ~8000 onshore UK seismic events from 1970-2012 from the British Geological Survey (BGS) earthquake database. They estimated that ~21% were anthropogenic, predominately caused by coal mining. Up to the date of their study, two earthquakes $M_L \geq 1.5$ had been caused by hydraulic fracturing. These two earth tremors, measuring 1.5 and 2.3 on the Richter scale were registered at Preese Hall near Blackpool, Lancashire. They were reported to have been caused by hydraulic fracturing in the area (Clarke et al., 2014). In 2018 and 2019, further hydraulic fracturing was undertaken by Cuadrilla Resources Ltd. at the nearby Preston New Road site near Blackpool.

57 and 137 events were recorded and located in 2018 and 2019, respectively, using several surface sensors operated by the British Geological Survey (BGS), Cuadrilla Resources, and University of Liverpool. Earthquake magnitudes were determined using the revised M_L scale developed by the BGS (Luckett et al., 2018), which extends the validity of existing UK-wide M_L

scale to a distance of less than 10-20 km. The dense station spacing and high-quality recordings enabled detection of very low magnitude micro-seismicity below 0.0 M_L. Tens of thousands of even smaller events were also detected on downhole microseimic instrumentation. The instruments that were used typically record continuously in three orthogonal directions (vertical and two horizontal) at sample rates of 100 or 200 samples per second.

According to the UK government's regulation to control induced seismicity, the Oil and Gas Authority should follow the use of a traffic light system (TLS). The TLS system defines three stages of action: green for normal operation, amber for magnitude between 0- 0.5 M_L, and red ($M_L \geq 0.5$) at which point well operation is suspended until the detailed analysis is undertaken. A 1.5 M_L earthquake was recorded as the biggest event in 2018 and the volume of fluid pumped was reduced as a consequence. The biggest event in 2019 was 2.9 M_L was felt at the surface.

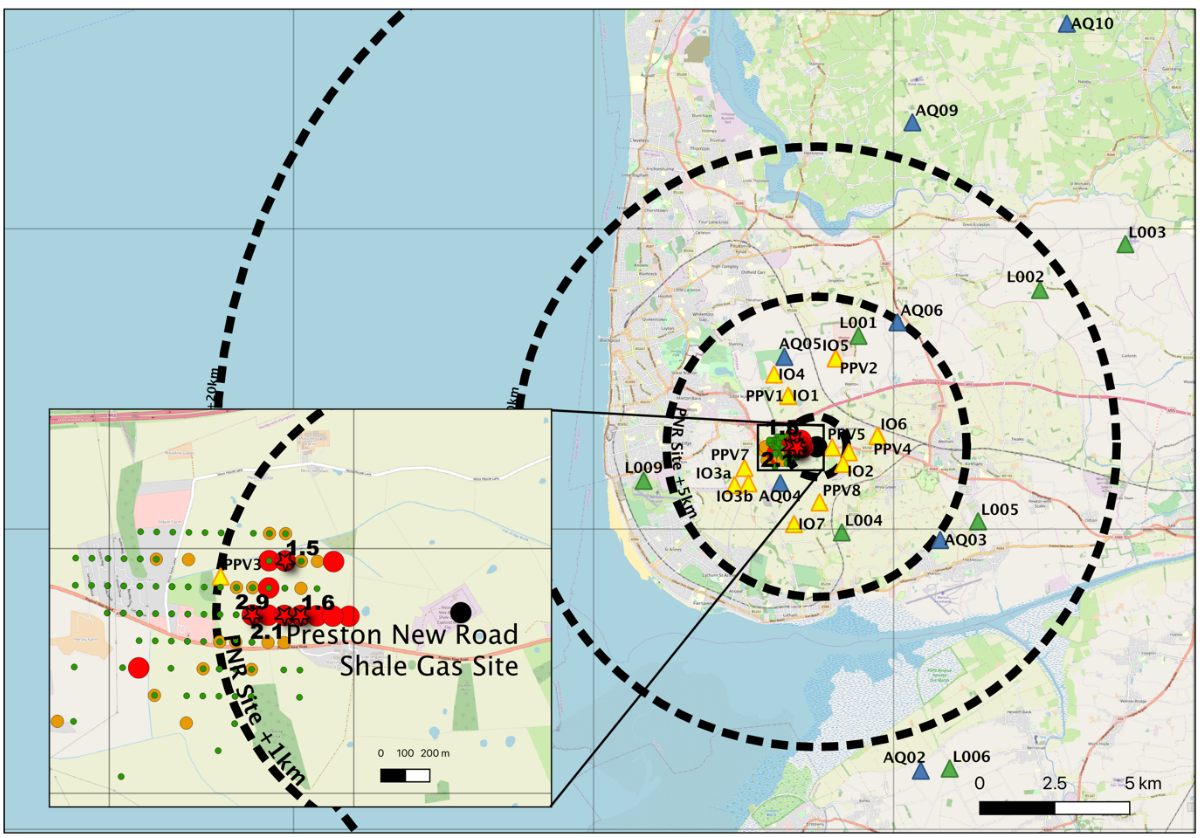

Figure 1 Map showing location of seismic monitoring stations (yellow: Cuadrilla, Green: University of Liverpool, and Blue: BGS), detected seismic events based on TLS magnitude category (green dots: M_L<0; orange dots:0<M_L<0.5; red dots:0.5<M_L; and red stars corresponds with biggest event for 2018 (1.5M_L at 11/12/2018), and 3 other biggest events in 2019 (on 21,24,26/8/2019 with magnitude 1.6,2.1,and 2.9 M_L respectively). Inset: zoom on epicentral region (modified after Edwards et al., 2019).

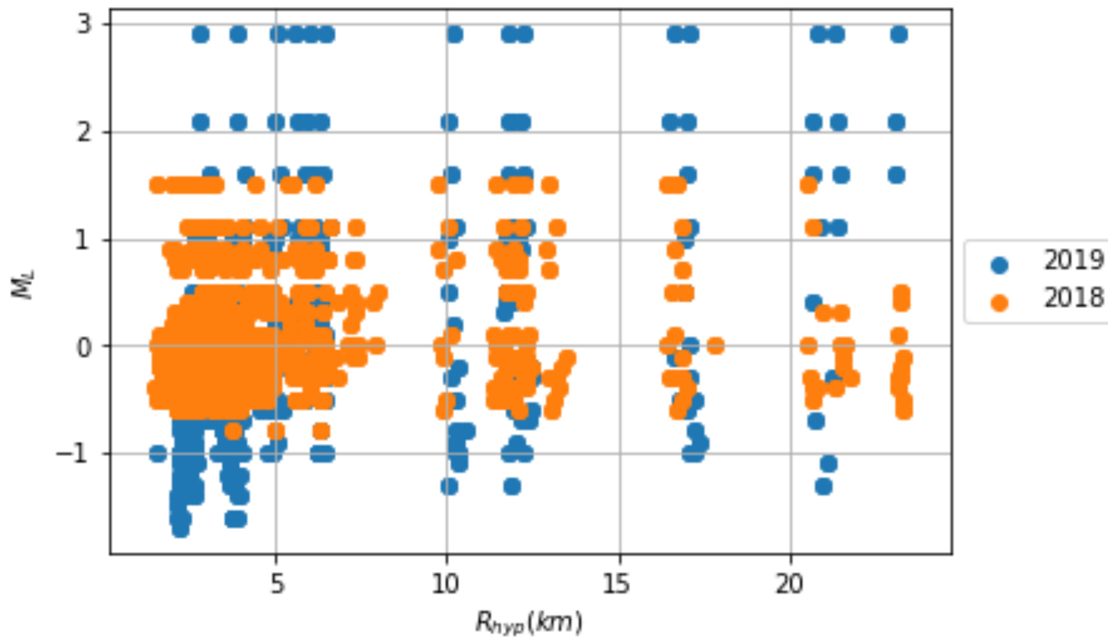

Figure 2 Magnitude-distance distribution of PNR database (2018-2019).

III. Overview of Ground Motion Models

a. Ground Motion Characteristic

Ground motion is a primary interest in seismic hazard analysis which shows the transient movements of the surface as seismic waves radiated by the earthquake passed by. Earthquake ground motion can be recorded using an accelerometer or seismometer and characterized based on the duration of shaking, point measures of peak acceleration, velocity, or displacement, frequency content, and the variability characteristic in terms of event-to-event, site-to-site and also spatial correlation. The ground motion resulting from an earthquake of a given size and distance is characterized by a predictive framework called ground motion prediction equation (GMPEs) as a simple ground motion model (GMM) that predicts the level of ground shaking and the associated uncertainty at a given location based on magnitude, distance, local site condition, etc. GMPEs for induced seismicity should provide a robust prediction for small and shallow earthquakes at close distances.

Past ground motion studies for seismic hazard in the UK have used GMPEs for stable continental regions as well as GMPEs for active crustal regions. However, since earthquakes in the UK are characterized by their comparatively small magnitudes, selection of appropriate GMPE will be tricky. Direct extrapolation for this particular small earthquakes data often leads to unsatisfactory prediction (Rietbrock et al., 2013). For example, significant deviation is observed between the available recording of Groningen ground motions and predicted PGA and PGV values from ground motion model developed for a neighbouring field, at Rowinskel (located 50 km away in the South East from the Groningen gas field) (Dost et al., 2004). The predicted values severely overpredict the recorded peaks (Bommer et al., 2017). As explained by Bommer et al. (2017) the main reason is a reliable ground motion model (GMM) needs to be developed specifically for the Groningen area rather than borrowing from other region was because the unusual upper crustal profile and the high-velocity of Zechstein salt layer above the reservoir which cause reflection and refraction of seismic waves. The stochastic method has been widely used as an alternative method to develop GMPEs in low seismicity regions. Rietbrock et al. (2013) derived GMPEs for the UK using 126000 simulated ground motion values from earthquake magnitude between $3 \leq M_W \leq 7$ at distances ranging from 1 to 300 km. The stochastic simulations were performed based on source and attenuation parameters determined by Edwards et al. (2008) using earthquakes with magnitude $2 \leq M_W \leq 4$. This approach has some limitations due to systematic differences in source parameters from larger earthquakes and smaller events.

Differences in source parameter or stress drop between tectonic and induced earthquake is still debateable, some of previous studies found similar range of stress drop (e.g. Huang et al., 2016,2017; Zhang et al., 2016; Ruhl et al., 2017), while others not (e.g. Abercrombie & Leary, 1993; Hough, 2014; Hough & Page, 2015; Boyd et al., 2017). According to Hough (2014), there is a significant systematic discrepancy in source properties between natural and induced events. Besides that, the study explained that induced events showed smaller intensities than predicted except for results at distances less than 10 km. Other studies examined that high-frequency ground motions depend on stress parameters and have lower stress parameters compared to natural earthquakes (Yenier and Atkinson, 2014; Atkinson, 2015; Novakovic and Atkinson, 2015; Yenier et al., 2017). Therefore, a robust GMPEs specific to the region of interest is preferred for cases of induce seismicity.

Atkinson (2015) developed a GMPEs specifically designed for the magnitude- distance range of induced seismic events. This GMPE was developed primarily from Californian earthquake data with magnitudes ranging between 3-6 at distances of less than 40 km, as these tend to be the magnitudes and distances at which these events can be felt. The GMPEs use hypocentral distance as the distance metric, which is more appropriate for small induced events than fault-based distances. Atkinson (2015) noted that if ground motions from induced events are compared to those from deeper natural events, the induced motions will appear higher (i.e. stronger shaking) at close distances and lower at further distances, due to the effects of shallow focal depth and stress parameter scaling on the ground-motion amplitudes.

Several important considerations for selecting GMPEs for induced seismicity has been noted by Bommer and Edwards (2018), summarised as:

1. Considering the close proximity to population centres, the risk of induced seismicity typically considered as smaller magnitude compared to tectonic events therefore in some cases, the extrapolation of GMPEs to smaller magnitudes will lead to over-estimation of the predicted amplitudes.
2. Induced seismicity tends to occur at shallow depths (< 4 km) compared to tectonic seismicity (around 10 km). Due to the proximity to the surface, the ground motion will be higher than for an equivalent tectonic event at greater depths. In contradiction, because of the shallow depth and lower confining stress, the stress drop may be lower and causing lower ground motion compared to ground motion from the deeper events.
3. Induced seismicity hazard focussed in the near epicentral region, therefore near-field prediction and shallow depth sources should be taken into account by using distance measures such as hypocentral or rupture distance.
4. Flattening of the attenuation curves at short distances as near-source saturation phenomenon. Distance saturation is dependent on the magnitude with a flattened part of the attenuation curve extending over a greater distance from the source for larger earthquakes.
5. It is important to have suitable GMPEs for the V_{s30} in the region since it will give significant differences in predictions.
6. Some predictor variables give relatively minor changes in prediction and not considered as important as other predictor variables described above. Therefore, it is better to assume a simple model form that can be easily adjusted.

b. Prediction of Ground Motions

A number of reviews and summary about ground motion estimation studies have been made in the past. The newest review by Douglas (2019) provides summary details of studies for PGA, PGV and response spectra published (as found in journals, conference proceedings, technical reports, and some PhD theses) between 1964 and late 2019. It summarizes, in total, 462 empirical

GMPEs for the prediction of PGA and 299 empirical models for elastic response spectral ordinates prediction. Another summary published by Stewart *et al*. (2015) presents a GMPE selection procedure that evaluates multidimensional ground motion trends, examines functional forms, and quantitative tests of GMPE performance for stable continental regions, subduction zones, and active shallow crustal regions. As explained above, ground motion is affected by complex process, and could be different due to the specific near surface condition, different geology structure, and earthquake mechanism itself. Therefore, ground motion might be different from one region to another. At Preston New Road, a review conducted for the UK Oil and Gas Authority (Edwards et al., 2019) focused on GMPEs from Atkinson (2015) and Douglas et al. (2013) which are commonly used for predicting ground motion due to induced seismicity.

Atkinson, 2015

GMPEs from Atkinson (2015) were specifically developed to help evaluate seismic hazard from induced seismicity. The model is developed using events of M 3 to 6 at hypocentral distances less than 40 km from the NGA-West2 database. The model is described to the functional form:

$$\log Y = c0 + c1M + c2\,M^2 + c3\log R + B(\tau) + W(\varphi) \qquad (1)$$

where Y is the ground motion parameter, logs are in base 10, $B(\tau)$ and $W(\varphi)$ describes the between- and within-event variability, M is moment magnitude and R is an effective point-source distance that take into accounts the near-epicenter saturation of motions, expressed as:

$$R = \sqrt{({R_{hyp}}^2 + {h_{eff}}^2)} \qquad (2)$$

where R_{hyp} is the hypocentral distance and h_{eff} is near-epicenter saturation of motions. h_{eff} value used in the analysis for PNR dataset suggested by Bommer and Edwards (2018), written as:

$$h_{eff} = \max\left(1, 10^{-0.28+0.19M}\right) \qquad (3)$$

The predictions were calculated using near-surface shear-wave velocity reference of 760 m/s, which corresponds to rock. The coefficients of Eq.1 denoted as c0, c1, c2, and c3 were determined by Atkinson (2015) using maximum likelihood regression method. One of the advantages of this model compare to model by Douglas et al. (2013) is the simplicity of the selected functional form which restrict its applicability to distance less than 50 km. In this case, the attenuation term only modelled as linear in log R without curvature on the slope due to growing anelastic effects at larger distances. Therefore, this formula (Eq.1) has some limitations if the objective is for regional distance applications or comparison with datasets over a wider distance range.

Douglas et al., 2013

Douglas et al. (2013) investigate ground motions generated by induced earthquakes and particularly those associated with geothermal or enhanced geothermal systems (EGSs). Douglas et al. (2013) suggested that differences in source, path and site conditions were the likely cause of region-specific differences. One model was produced without correction for site effect and one with corrected to a reference rock with V_{s30} = 1100 m/s. The dataset included events with magnitude 1 to 4 at distances up to 20 km. GMPEs by Douglas et al. (2013) formed as:

$$\ln Y = a + bM + c \ln R + dR_{hyp} + B(\tau) + W(\varphi) \qquad (4)$$

where Y is the ground motion parameter, M denotes the moment magnitude, R is the point-source distance explained in Eq.2, R_{hyp} is the hypocentral distance, and $B(\tau)$ and $W(\varphi)$ describe the variability. Key differences from this model with Atkinson (2015) are the use of natural logarithms rather than base-10, and the lack of M^2 term. Coefficients of a, b, c, and d were obtained by the authors using regression analysis, with b indicating the magnitude scaling of the derived GMPEs and suggesting a comparable magnitude scaling of induced, mining, and natural seismicity (Douglas et al., 2013; Douglas and Jousset, 2011). The regression coefficient of c and d are non-unique and may correlate one another. Both coefficients imply a fast decay with distance that represent geometrical spreading and intrinsic attenuation which are difficult to be distinguished clearly.

c. Summary of Previous Ground Motion Predictions for PNR Dataset

A previous study about ground motion models for Preston New Road (PNR) was carried out by Edwards et al. (2019) adapting from Atkinson (2015) and Douglas et al. (2013), as common GMPEs used for predicting ground motion from induced seismicity. Since both GMPEs developed using moment magnitude (M_W) while the PNR catalogue provide magnitude as local magnitude (M_L), then it is necessary to convert M_L to M_W. Two conversion models were tested by authors:

Grünthal et al. (2009) as M_W-M_L conversion based on tectonic of European events and Edwards et al. (2015) which is in accordance to empirical data of PNR-1z presented by Cuadrilla Resources (2019b). The assessment of GMPEs for PNR ground motions was done by comparing the residual PSA, PGA, and PGV using both GMPEs (Atkinson, 2015 and Douglas et al., 2013) along with the magnitude conversion from M_L to M_W of Grünthal et al. (2009) and Edwards et al. (2015).

According to the Edwards et al (2019), the best approach for predicting ground motions from PNR-1z seismicity is to use the Atkinson (2015) with magnitude conversion based on Edwards et al. (2015). Even though GMPEs from Atkinson (2015) was developed using magnitude>3, it performs well consider that Atkinson (2015) used a more complex functional form, including M^2 term and magnitude dependent near-field saturation. The authors further note that for predicting ground motions from larger events at PNR (M_L>2.5) the GMPEs from Atkinson (2015) should be used with M_L to M_W of Grünthal et al., (2009).

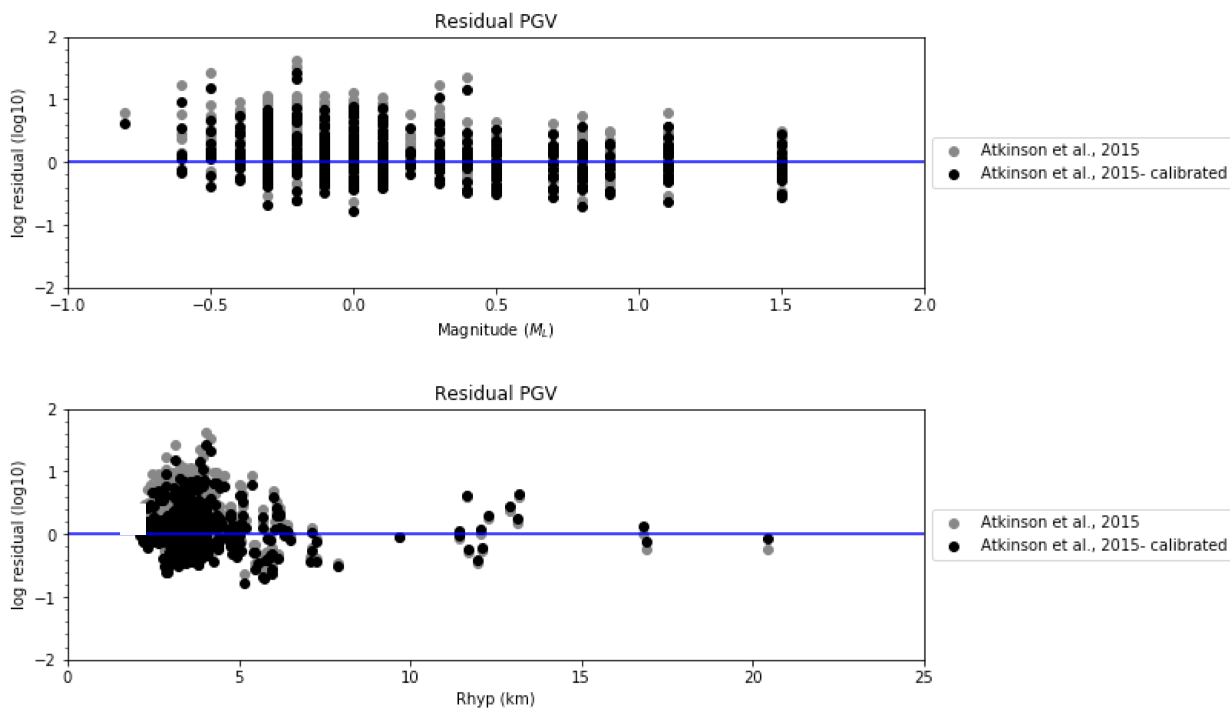

Figure 3 Residual plot from Atkinson (2015)- M conversion using Edwards et al., (2015). (adapted from Edwards et al., 2019)

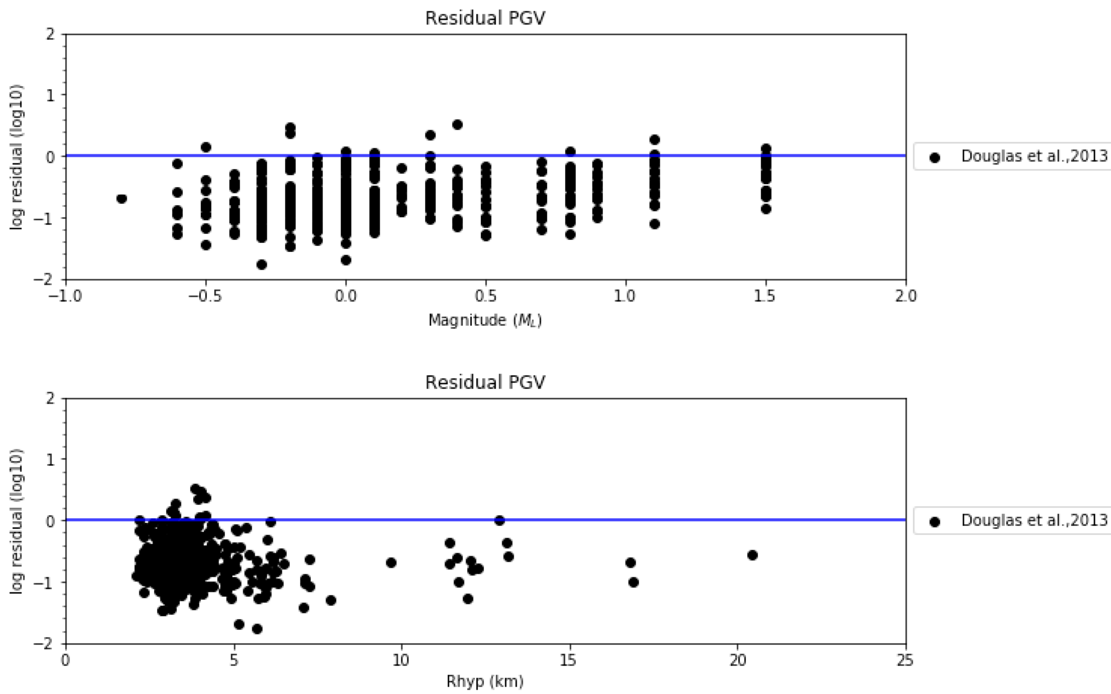

Figure 4 Residual plot from Douglas et al., (2013)- M conversion using Edwards et al., (2015). (adapted from Edwards et al., 2019)

Interesting discussion is also found in regard to Figure 3 and 4, where residual PGV values (in log 10 unit or factor of 10) from Atkinson (2015) are positive and shows the underprediction of the observations PGV values while the Douglas model exhibit contrary behavior with overprediction PGV values. A standard deviation (σ_{total}) of 0.33 is estimated for PGV. In both figures, the residual value decreases with the increasing magnitude and distance which shows that the discrepancy of PGV values is more clearly seen at a closer distances (and to some extent at smaller magnitude). These results also indicate an unsatisfactory sigma between predicted-observed values, particularly considering the 'single-source-zone' nature of the induced seismicity. These disparities clearly justify additional effort to improve ground motion models for Preston New Road.

IV. Toward New Ground Motions Prediction Equations

Ground motion recorded in each station can be seen as the combination of three contributions: source characteristics, wave propagation (geometrical, intrinsic attenuation, and scattering effect), and site responses. Generally, GMPEs are the simplified model which deal with all three aspects. It is typical that ground motion cannot be described in detail considering the complexity of the process that occurs. This is due to the lack of information (e.g., about the rupture, the crustal structure and the near-surface effects) and the nature of the simplifications inherent in GMPEs. Therefore, to determine the variability of ground motion affect by each aspect, the separation into physical source, path, and site term will be followed in this study project.

a. Earthquake Magnitude

Source terms in ground motion models (GMMs) are typically represented by the earthquake magnitude and stress drop. An earthquake's moment magnitude can be described as the earthquake's 'size' and relate to physical characteristics of the fault/ crack that generated seismic waves denoted as M_W. The moment magnitude (M_w) scale, is uniformly applicable to all sizes of earthquakes and more directly related to the energy of an earthquake than other scales, also does not saturate but it is more difficult to compute. Meanwhile, the local magnitude (M_L), also known as the Richter scale, is still widely used in different part of the world, because it easier to calculate. It describes the surface effects, normalized to a common reference distance, without consideration of the physical source. Different magnitude scales are usually calibrated to be consistent with one another. Several different models have been proposed to convert between M_L and M_W developed from different type of datasets. Grünthal et al. (2009) define a relationship between M_L - M_W over a wide magnitude range. Meanwhile, model proposed by Edwards et al. (2015) and Cuadrilla Resources (2019b) obtained from magnitude < 2 show that moment magnitude of induced earthquakes at PNR are systematically higher than local magnitude. This is consistent with numerous other studies of both induced and tectonic events (e.g., Dost et al, 2018) and is due to the fact that path (attenuation) effects band-limit the high frequency motions of small events (Deichmann, 2017).

Here we present an updated model of M_L - M_W relationship for the PNR dataset based on direct calculation of M_w for selected events. After removing the instrument response and applying cosine taper, S-Coda wave and noise windows are defined. The signal window (in this case from beginning of S-wave until the end of coda window) and noise window are transformed into the frequency domain using multitaper spectral estimation techniques (Prieto et al., 2009). Henceforth, records were selected based on signal-to-noise ratio (SNR>2).

The signal displacement spectrum $A(f)$ recorded in one station can be written a product of a source term $\Omega(f)$, attenuation term $P(R,f)$, and site effect term $S(f)$:

$$A(f) = \Omega(f) * P(R,f) * S(f) \qquad (5)$$

where R is the hypocentral distance and f is the frequency. In this study, we assume the site effect is uniform therefore we neglect $S(f)$. For a source model, the Brune (1970) model is chosen, combined with the path/ attenuation term can be expressed as:

$$\Omega(f) * P(R,f) = \frac{\Omega_0 e^{-(\pi f^{1-\alpha} t^*)}}{1 + (f/f_c)^2} \qquad (6)$$

in which Ω_0 is the low- frequency plateau, f is the frequency, f_c is the corner frequency and t^* is the attenuation parameter ($t^* = T/Q_0$, with T the travel time and Q the path-average quality factor). The Ω_0 term contains geometrical spreading, radiation pattern, seismic moment, and other frequency–independent effects. An inversion process is applied to fit t^*, f_c, Ω_0, and α (if we consider frequency-dependence of Q; otherwise $\alpha = 0$) with the model defined in Eq. 5 and 6.

The seismic moment (M_0) of a seismic record can be written as:

$$M_0 = \frac{4\,\pi \rho v^3 R_{hyp} \Omega_0}{F_s\, R_{\theta\phi}} \qquad (7)$$

where ρ is the rock density at the source ($2800\, kg/m^3$), v is the velocity in the source ($v = 2000\ \mathrm{m/s}$), R_{hyp} is the hypocentral distance, and Ω_0 is the low- frequency plateu. F_s is Free surface amplification factor ($F_s = 2$ for normally incident SH waves and a good approximation for SV) and $R_{\theta\phi}$ is the average radiation pattern coefficient for S-wave (0.55) (Boore &Boatwright, 1984).

From the relationship between M_0 and M_W, we can calculate M_W :

$$M_W = \frac{2}{3} \log M_0 - 6.03 \qquad (8)$$

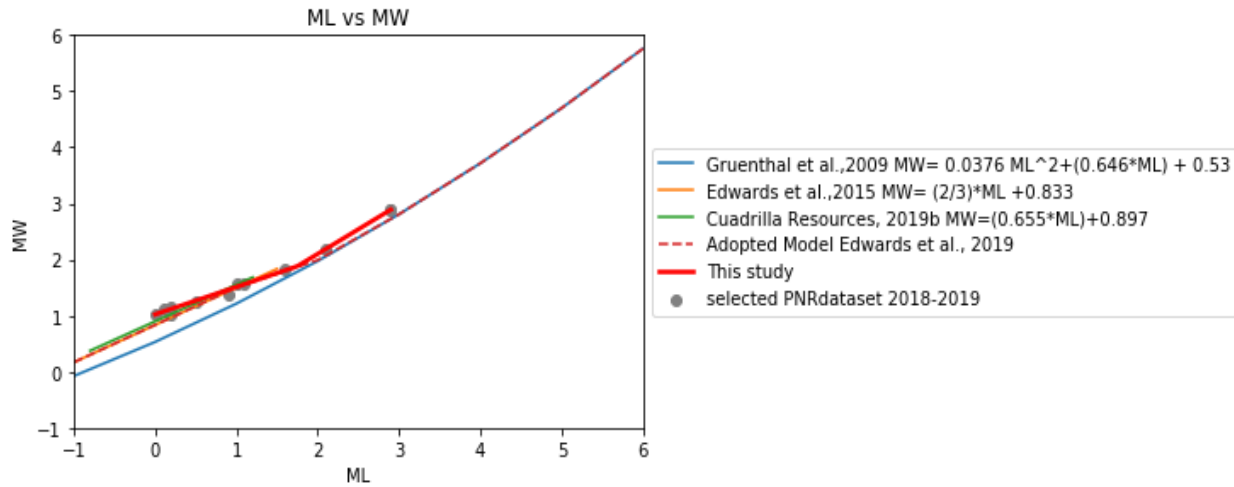

Figure 5 Local to moment magnitude conversions

Bi-linear regression performed to fit the scattered M_W for selected PNR dataset, and can be summarized as:

$$M_W = k1(M_L - 1.749) + 1.88 \quad \text{for } M_L \leq 1.749 \qquad (9\text{ a})$$

$$M_W = k2(M_L - 1.749) + 1.88 \quad \text{for } M_L \geq 1.749 \qquad (9\text{ b})$$

where $k1 = 0.4907$ and $k2 = 0.8774$ are the slopes of regression line. This new model supports the use of Edwards et al. (2019) model (dashed red line) for magnitude range between 0-3. However, if we extrapolate the new model (red line) below 0 M_L or upper 3 M_L, it will give higher M_w respected to M_w from model by Edwards et al. (2019). Therefore, we need more data to justify the reliability of this model.

b. Stress Drop

Besides magnitude, dynamic stress drop can help us to characterize a seismic event and can be considered to represent energy release. During a seismic event, the dynamic stress drop implies a significant impact on the radiated wavefield. There are various ways to calculate stress drop, but as used in engineering seismology stress parameter effectively defines the proportion of high-frequency radiated energy for a given magnitude. Higher stress drop events emit a greater proportion of high frequency energy.

Stress drop defined as static measure describing the average stress acting on fault before and after rupture (Kanamori, 1977; Hanks, 1979; Boore, 1983). In this case, information regarding the size of the rupture is needed. However, for small earthquakes, direct observations of the rupture geometry are not possible so the fault dimensions must be estimated from far-field observations of the radiated seismic waves. Therefore, the methods of estimating stress drop for small earthquakes derived under assumptions about the dynamics of the source, they are sometimes termed as "dynamic stress drop" or "Brune stress drop" (Brune, 1970; Shearer, 2009; Holmgren et al., 2019). Hough (2014) infers that induced earthquakes have lower stress drops than tectonic earthquakes based on a comparison of non-instrumental "Did You Feel It?" intensities. Other studies explained that induced earthquake sequences may have comparable stress drops to tectonic earthquakes (Huang et al., 2016,2017; Zhang et al., 2016; Ruhl et al., 2017). Huang et al. (2017) suggests that ground motion prediction equations developed for tectonic earthquakes can be applied to induced earthquakes after properly considering the effects of depth and faulting style. This argument is supported with their findings that in the strike-slip dominant area (central United States) shows a comparable median stress drop of induced seismicity to the tectonic earthquakes. On the other hand, in North America, which exhibits dominantly reverse faulting, a lower median stress drop of induced earthquakes is observed with respect to tectonic earthquakes. Earthquake stress drop also often considered depth-dependent, with deeper earthquake leads to higher stress drop (Edwards et al., 2019; Huang et al., 2017). According to Huang et al. (2017), the depth dependence of stress drop estimates suggests that more intense ground motions are expected from deeper earthquakes for a given hypocentral distance (deeper earthquake generate higher stress drop). Since GMPEs are usually developed using predominantly deep tectonic events, in some cases where the stress drop of induced earthquakes is not comparable with the stress drop from tectonic earthquakes, predictions will overestimate ground motions when applied to shallow induced earthquakes. It is therefore important to consider both the effects of depth-dependent stress drops and propagation effects for predicting ground motions of induced earthquakes.

c. Attenuation

Seismic ground motions will decrease as the increasing distance from the source, partly for geometric reasons because their energy is distributed on an expanding wave front, and partly because their energy is absorbed by the material they travel through. Geometrical decay is due to the fact that energy must be preserved over an increasing large surface, means that amplitude must be decrease proportional to distances. When seismic waves propagate beneath the surface, the waves not only lose energy through geometrical spreading effects but also through intrinsic and scattering attenuation. Intrinsic attenuation accounts for the seismic energy which converted into different energy types (e.g., heat), and scattering attenuation describes the redistribution of seismic energy into different directions. Usually for simplification, geometrical decay and attenuation modelled as:

$$G(f) = \frac{exp^{-\pi f\, R/_{\beta\, Q(f)}}}{R^{\lambda}} \tag{10}$$

where R is the hypocentral distance, β is the average shear wave velocity, Q is the quality factor and λ is the rate of geometrical spreading. For shallow induced seismicity, near-field motions tend to decay more rapidly than 1/R (Edwards et al., 2019; Atkinson, 2015; Butcher et al., 2020; Ameri et al., 2020).

Measurements of seismic attenuation (Q^{-1}) can vary considerably when made from different part of seismograms or using different techniques, especially at high frequencies (Sarker & G.A. Abers, 1998). Such differences could be methodological or may reflects earth processes. In this study, the measurement was made for different signal window (S-wave, coda wave, and S-coda wave) utilizing two different approaches: (1) parametric fit to spectral decay, and (2) coda envelope decay with time. The parametric fit to spectral decay observed using 3 different signal windows mentioned above, while coda envelope decay with time was applied only for the coda wave window. For the parametric fit to spectral decay methods, attenuation along with source parameters can be inverted in a parametric scheme. A spectral fitting method was performed using horizontal component (east-west (E) and north-south (N)) of 194 events recorded in Preston New Road in 2018-2019. However, only recordings with good signal-to-noise ratio (SNR> 3) will be considered. Processing time series data such as removal of instrument response, detrending, tapering signal, determining noise and signal windows (S-wave, coda wave, or S-coda wave) were performed before the calculation of Fourier spectra. The spectral of chosen signal window and noise window then calculated using multitaper spectral estimations method. After that, the signal-to-noise ratio (SNR) was calculated and lower and upper frequency bound was determined. Only recordings with good quality of SNR (SNR> 3) will passed to the spectral fitting step. An inversion approach to fit model described in Eq. 6 was performed for four defining parameters: Ω_0, f_c, α, and t^*. The methods allow us to calculate both frequency-independent and frequency-dependent t^* measurements. Frequency dependent of Q is considered by parameterizing t^* as:

$$t^*(f) = \; {t_0}^* \, f^{1-\alpha} \tag{11}$$

where ${t_0}^*$ represent t^* at f= 1 Hz and α describes frequency dependency.

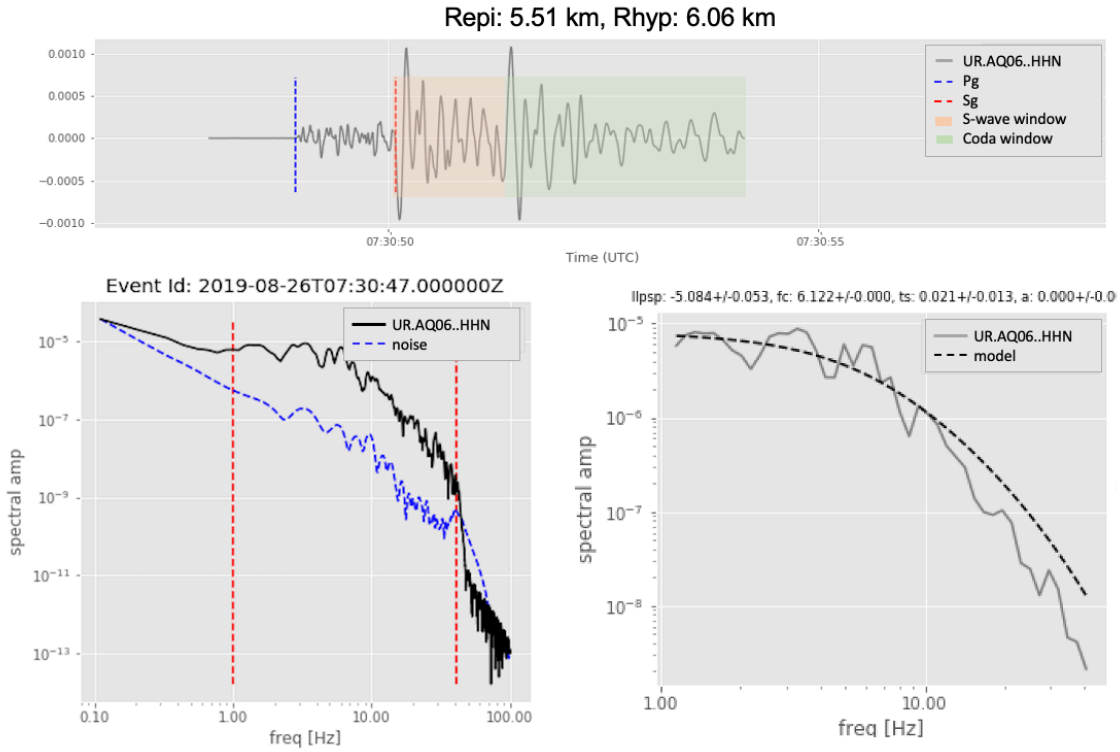

Figure 6 Example of spectral fitting process: (Top) S-wave and coda time windows, (Bottom left) Fourier amplitude spectra of signal and noise, and (Bottom right) spectra fitting from ML 2.9 event occurred at 26/08/2019 recorded in the north-south component of station UR.AQ06.

An alternative method using coda envelope decay with time can be inverted for apparent attenuation and can be done by assuming single scatter or multiple scattering model. For simplicity, in this work we assume single scattering model as expressed below:

$$A(f,T) = \; A_0(f)T^{-\upsilon}e^{-\pi f T/Q_{clt}} \tag{12}$$

where ${Q_{clt}}^{-1}$ is the coda attenuation which is assumed to vary with frequency in a manner identical to t^* in Eq.11, A_0 represents source factor that includes as independent contributor for attenuation, f is the frequency, T is lapse time since the time of occurrence/ earthquake origin time, and υ is a positive constant that is related to geometrical spreading (Aki and Chouet, 1975), in this study υ=1, which represent the spherical spreading of body wave.

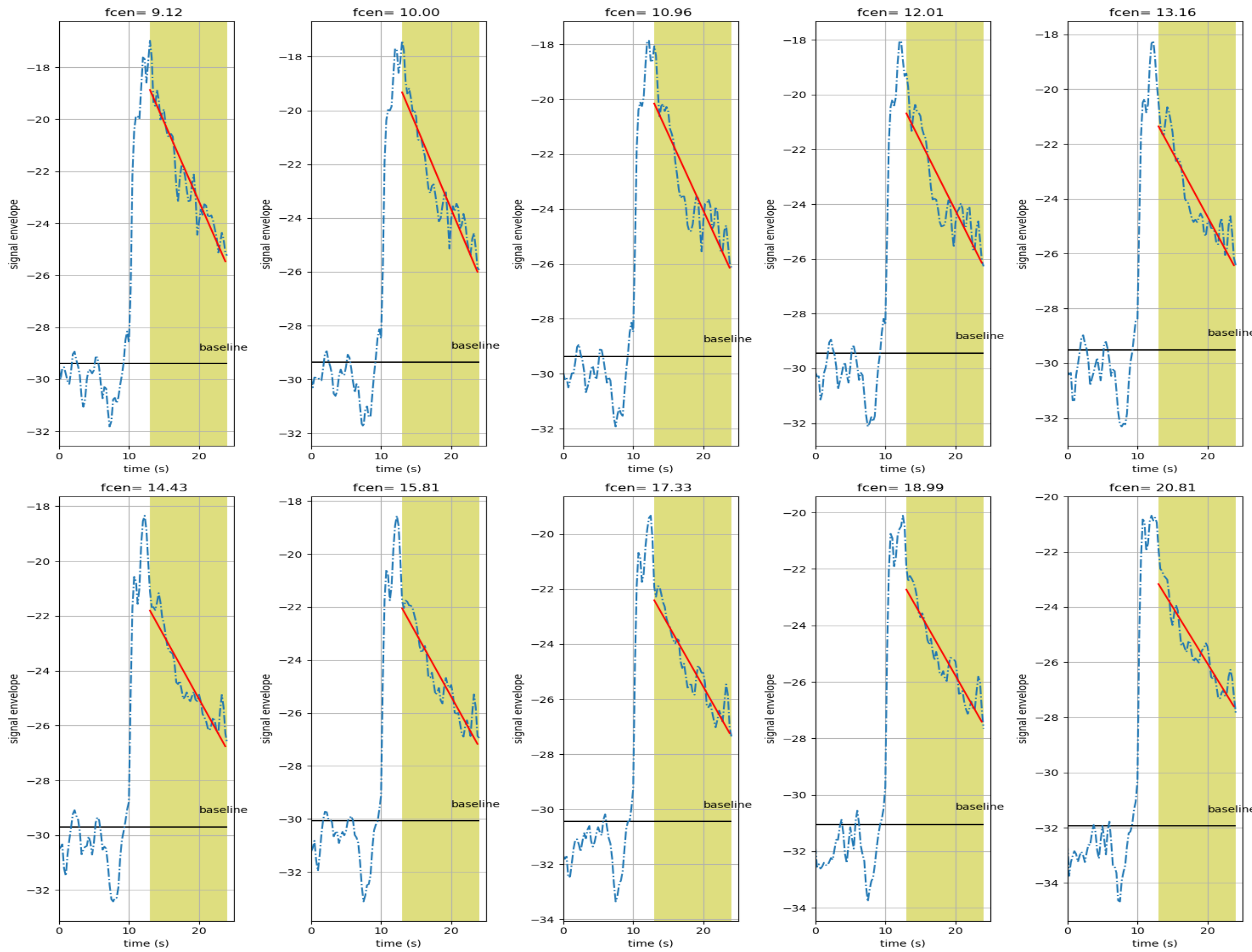

Figure 7 Example of coda envelopes obtained as well as linear regression $Q_c\ (f)$ (red line) for 10 different central frequencies in bands [10-25 Hz]. Noise baseline is shown as a horizontal black line and coda windows displayed as yellow rectangle.

There are some limitations in the application of Q calculation using coda envelope decay technique found in this study. Due to the shallow and short duration records available, there is a probability that coda waves are not being captured well. An adjustment has been made for defining coda lapse time (time lapsed after the origin time where the coda starts), and defined as $t_c = 1.4(\ t_s - t_p\ ) +\ t_s$ modified from the original version proposed by Perron et al. (2017) which model the beginning of coda as $t_c\ = 2.3(\ t_s - \ t_p\ ) +\ t_s$. The time lag between the end of S-wave and the beginning of coda is very short and may affect noise contamination and the influence of S-wave in the coda window. Smaller windows give less stable results, particularly at low frequencies. Therefore, the Q_{clt} were observed for 10 frequencies in the bands 10 – 25 Hz using four biggest events recorded from PNR dataset 2018-2019 (see Figure 1). Q_{clt} from individual recordings $Q_{clt(i)}$ were calculated using linear regression of slope of analytic signal which represent decay of coda envelope (Figure 7). Collection of $Q_{clt(i)}$ from all events then are used to calculate Q_{clt} evaluated at frequency of 10 Hz ($Q_{clt}(f = 10)$ or denoted as Q_{10} in Table 1) for different sensors which provided in Table 1 with mean Q_{10} value of 113.998 and standard deviation of 36.3. Estimation of mean-Q_{10} and mean- α may represent Q_{clt}value of PNR region, which modelled as $Q_{clt}\,(f) = 114(f/10)^{1.2}$. Lower Q_{10} values were found around epicentre of PNR site and directed towards the coastal area, while towards the northwest of the site, Q_{10} values seem increased. Thus, high attenuation indicated by lower Q_{10} values is likely to be associated with more sediment deposits and these tend to be coastal and river based (see Figure 8). Another model of Q_{clt} produced for PNR dataset by stacking $Q_{clt(i)}$ from all events stated as $Q_{clt}\,(f) = 110(f/10)^{1.04}$. Both $Q_{clt}\,(f)$ modelled in relatively upper crust layer (< 30 km), while the regional Q determined from multiply reflected shear waves (*Lg*) and correlate with large scale crustal features (up to 100 km or deeper). Therefore, obviously the local Q smaller than regional model for Britain $Q_{Lg}\,(f) = 266\,f^{0.53}$,which is modelled between 1 – 10 Hz frequency bands for regionally propagating Lg waves (Sargeant & Ottemöller, 2009).

Table 1 Q_{10} and α calculated in each station using the 4 biggest events recorded at Preston New Road

Station	Q10	alpha
LV.L001	76.4	0.83
LV.L002	111.0	1.32
LV.L003	191.5	1.88
LV.L006	76.8	1.74
LV.L009	118.6	0.34
UR.AQ03	81.0	1.23
UR.AQ04	81.8	0.79
UR.AQ05	71.0	0.78
UR.AQ06	87.4	1.21
UR.AQ07	169.1	1.48
UR.AQ09	115.4	1.21

Station	Q10	alpha
UR.AQ10	183.9	1.77
SD.IO1	106.1	0.78
SD.IO2	124.3	1.19
SD.IO3A	92.7	1.75
SD.IO4	120.1	0.75
SD.IO5	130.8	1.03
SD.IO6	113.9	0.9
mean	**114.00**	**1.17**
stdv	**36.29**	**0.43**
std error	**8.55**	**0.10**

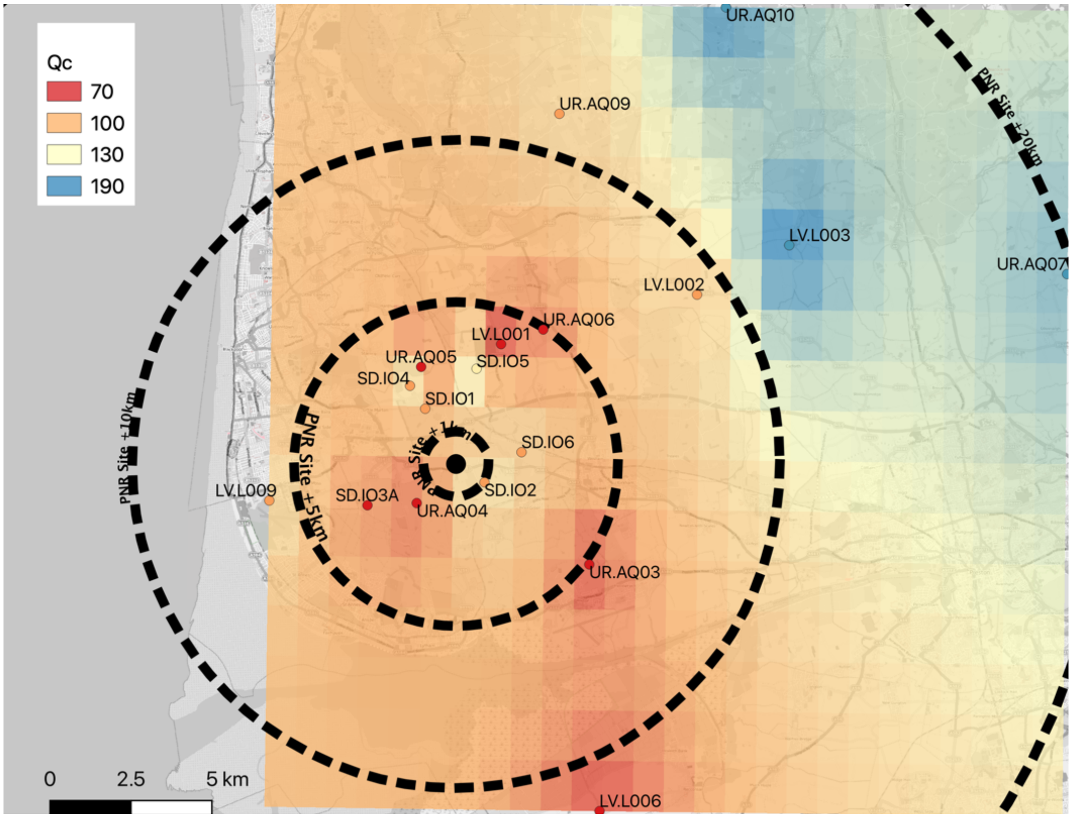

Figure 8 Map of Q_{clt} (f=10) calculated using coda envelope decay method

Frequency-independent Q is model obtained from spectral fitting techniques using three different seismic phase windows: S-wave, coda wave, and S-coda wave windows. Three Q models from different seismic windows show similar results with Q_s = 179.63, Q_c = 168.09 and Q_{sc} =215.96. Butcher et al. (2020) reported mean Q-value for the New Ollerton (UK) data (approx. 300 km from Preston New Road) is 116. This frequency-independent Q was calculated from 305 seismic events with magnitude ranging between -0.7< M_L< 2.1 recorded from 7 broadband seismometers installed near New Ollerton, UK to investigate mining-induced seismicity. The amplitude spectrum of each individual events was generated and inverted for their best-fitting of Q by combining κ_0 with a Brune source model. Butcher at al. (2020) suggest that the spectral fitting method is more likely to give frequency-independent Q since intrinsic attenuation is dominant and the short signal windows do not really account for the influence of scattering, particularly at short distances.

d. Site Response

Site effects describe the local effect of uppermost layers of rocks and soil when the seismic waves propagating through them. The differences of the ground motion due to the Earth structure below the site can be related to different factors, in general, the main factor is the impedance contrast between the soil layers or soft sedimentary and the bedrock. The impedance contrast determines how strong the waves are at particular frequencies.

In general, there are two approaches to estimate the site effect using experimental methods: (1) reference site and (2) non-reference site techniques (Bard,1995). The reference site method (RSM) estimated by comparing records at the nearby sites, using one as the reference site. It is assumed that records from the reference site (in general a station installed on outcropping hard rock) contain the same source and propagation effects as records from the other sites. Therefore, differences observed between the sites are explained as being due to the local site effects. However, a major drawback of these methods is that a suitable reference site may not always be available. In order to overcome this disadvantage, non-reference site techniques such as the horizontal-to-vertical (H/V) spectral ratio method are widely used.

In this study, we examined H/V spectral ratios using ambient seismic noise ($HVSR_N$) also earthquake recordings ($HVSR_E$) at 17 sites (9 Liverpool sites, and 8 BGS sites). The result of $HVSR_E$ calculated by taking the whole recordings for each event recorded from three different components. Apparently, the result giving a close value of resonance frequency (f_0) and peak amplification (A_0) obtained from $HVSR_N$. The resonance frequency as a result of HVSR method can be related to a simple model in terms of a layer over half-space that approximated as:

$$f_{r,0} = \frac{V_s}{4H_B} \tag{13}$$

where V_s is the shear waves velocity of the overlying layer and H_B is the depth of bedrock layer (Hassani and Atkinson, 2016). By taking the estimates of bedrock depth from BGS superficial deposits thickness model reported by Edwards et al. (2020), and assuming the bedrock shear-wave velocity (V_{sb}) as 1500 m/s, we can calculate V_{s30} as:

$$V_{s30} = \frac{30}{\frac{1}{4f_o} + \frac{\max(0, 30 - H_B)}{V_{sb}}} \tag{14}$$

A comparison of V_{s30} calculation from several observation that has been undertaken for PNR sites studies are presented in the Figure 9 and Table 2-3. Result from previous studies by Edwards et al.(2019, 2020) explained that site characterisation of PNR was performed using multi-channel analysis surface waves (MASW) at three different sites (L001, L003, and L009) and measurement of V_{s30} reported as 257 m/s for site L001, 240 m/s for site L003, and 205m/s for L009 (denote as red cross: measured V_{s30} in Figure 9). Besides measurement from shear-wave velocity profiles, estimation of V_{s30} also carried out using correlation of Rayleigh wave phase velocity dispersion of the 40-45 m wavelength signal (V_{s30}-dispersion proxy: shown as green cross in Figure 9).

The result of f_0 from our HVSR$_E$ observation then were used together with mean (H_mean) (represented as blue diamond), and maximum bedrock depth (H_max) (denote as orange box) to calculate V_{s30} following Eq.14. Meanwhile, the f_0 from HVSR$_N$ represented by V_{s30} calculated by Edwards et al. (2020) using mean of bedrock depth (legend in Figure 9: "H_mean Edwards et al.(2020)"). In addition, V_{s30} also estimated under the assumption of uniform bedrock at 30 m depth.

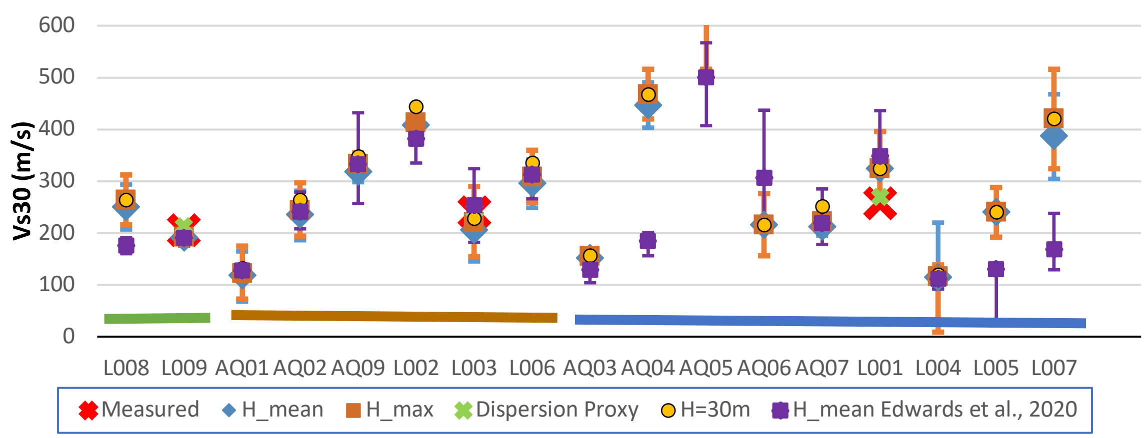

Figure 9 Estimated V_{s30} grouped by superficial geology (green: blown-sand, brown: peat, and blue: till). Error bars based on the lower and higher estimates of f_0 (very small error bar for "Measured V_{s30}", please see Table 3.)

Wider variability of V_{s30} found in till ranging around 100- 600 m/s, while in peat ranging between 100-400 m/s and around 200-300 m/s for blown-sand. The estimated V_{s30} from f_0 are close to the measured values in three different sites (L001, L003, and L009). Compared to V_{s30} calculated using f_0 - HVSR$_N$ by Edwards et al. (2020), the calculated V_{s30} using f_0 from HVSR$_E$ is relatively larger at some sites (AQ04, AQ05, L005, and L007) which could be influenced by the quality of signal used in the HVSR$_E$ analysis.

548

Table 2 V_{s30} calculated using combinations of mean/ max bedrock depth and f_0 and its upper/ lower estimates.

					This study										
					f0 selected				Vs30 Estimates (m/s)- This Study						
Name	Net	Geology	Bedrock Depth [Mean] (m)	Bedrock Depth [Max] (m)	f0 (Hz)	f0 low (Hz)	f0 high (Hz)	f0 Quality	Vs30 (H_mean, f0)	ΔVs30 (H_mean, f0_low, f0_low)	ΔVs30 (H_mean, , f0_high)	Vs30 (H_max, f0)	ΔVs30 (H_max, f0_low)	ΔVs30 (H_max, f0_high)
L008	UOL	BLOWN SAND	24	32	2.2	1.8	2.6	Clear	176	15	16	182	16	17
L009	UOL	BLOWN SAND	29	30	1.6	1.5	1.7	Clear	191	13	16	193	13	16
AQ01	BGS	PEAT	4	11	1.1	0.6	1.6	Clear	127	11	11	131	11	11
AQ02	BGS	PEAT	16	21	2.2	1.7	2.7	Clear	241	38	33	251	40	36
AQ09	BGS	PEAT	22	26	2.9	2.7	3.1	Moderate	332	100	75	348	108	83
L002	UOL	PEAT	24	25	3.7	3.4	4	Clear	382	64	47	387	66	48
L003	UOL	PEAT	16	26	1.9	1.3	2.5	Moderate	254	70	72	278	82	88
L006	UOL	PEAT	18	22	2.8	2.3	3.3	Clear	313	22	47	327	23	52
AQ03	BGS	TILL	25	29	1.3	1.3	1.3	Clear	129	12	25	131	12	26
AQ04	BGS	TILL	27	34	3.9	3.5	4.3	Broad	184	17	28	187	18	29
AQ05	BGS	TILL	33	37	8.4	4.3	12.5	Broad	500	67	93	500	67	93
AQ06	BGS	TILL	34	37	1.8	1.3	2.3	Broad	307	130	85	307	130	85
AQ07	BGS	TILL	8	14	2.1	1.9	2.3	Moderate	219	66	41	229	71	45
L001	UOL	TILL	31	36	2.7	2.1	3.3	Moderate	349	87	29	349	87	29
L004	UOL	TILL	19	21	1.0	0.8	2.0	Broad	111	14	19	111	15	19
L005	UOL	TILL	30	32	2	1.6	2.4	Broad	130	12	109	130	12	109
L007	UOL	TILL	24	31	3.5	2.7	4.3	Broad	168	70	39	174	74	42

Table 3 V_{s30} calculated using combinations of mean/ max bedrock depth and f0 and its upper/ lower estimates, also V_{s30} measured, V_{s30} from dispersion, and V_{s30} (H=30m) from Edwards et al. (2020)

					Edwards et al., (2020)												
										f0 selected- HVSRN				Vs30 Estimates (m/s)		
Name	Net	Geology	Bedrock Depth [Mean] (m)	Bedrock Depth [Max] (m)	Measured Vs30 (m/s) from Vs(z) (mean)	Measured Vs30 (m/s) from Vs(z) (16th-percentile)	Measured Vs30 (m/s) from Vs(z) (84th-percentile)	Vs30(m/s) = VR 40-45 (Dispersion)	Vs30 (m/s) uniform bedrock	f0 (Hz)	f0 low (Hz)	f0 high (Hz)	f0 Quality	Vs30 (H_mean, f0)	ΔVs30 (H_mean, f0_low)	ΔVs30 (H_mean, f0_high)
L008	UOL	BLOWN SAND	24	32					264	1.52	1.39	1.66	Very Clear	176	15	16
L009	UOL	BLOWN SAND	29	30	205.3	203.3	205.5	213	192	1.60	1.49	1.74	Very Clear	191	13	16
AQ01	BGS	PEAT	4	11					132	1.19	1.08	1.30	Very Clear	127	11	11
AQ02	BGS	PEAT	16	21					264	2.26	1.87	2.61	Clear	241	38	33
AQ09	BGS	PEAT	22	26					348	3.04	2.06	3.81	Moderate	332	100	75
L002	UOL	PEAT	24	25					444	3.45	2.83	3.91	Clear	382	64	47
L003	UOL	PEAT	16	26	240	237.3	244.3	244	228	2.41	1.68	3.21	Modera	254	70	72
L006	UOL	PEAT	18	22					336	2.99	2.75	3.51	Very Clear	313	22	47
AQ03	BGS	TILL	25	29					156	1.10	1.00	1.32	Clear	129	12	25
AQ04	BGS	TILL	27	34					468	1.56	1.41	1.80	Very Clear	184	17	28
AQ05	BGS	TILL	33	37					1008	4.17	3.61	4.94	Clear	500	67	93
AQ06	BGS	TILL	34	37					216	2.56	1.48	3.27	Broad	307	130	85
AQ07	BGS	TILL	8	14					252	2.18	1.44	2.68	Moderate	219	66	41
L001	UOL	TILL	31	36	257.1	251.7	264.4	269	324	2.91	2.18	3.15	Moderate	349	87	29
L004	UOL	TILL	19	21					120	0.96	0.83	1.13	Clear	111	14	19
L005	UOL	TILL	30	32					240	1.08	0.98	1.99	Broad	130	12	109
L007	UOL	TILL	24	31					420	1.45	0.84	1.80	Broad	168	70	39

These V_{s30} result later on can be mapped and observed respected to the geology map to characterize the site effect of PNR area. Despite that there is no universal agreement that V_{s30} is a valid proxy to determine seismic amplification which appears to be too complex to be related to the Vs profile in the first 30 meters alone, certainly there is a correlation between V_{s30} and site amplification (Castellaro et al., 2008; Hartzell et al, 2001).

Aside from amplification effect of decreasing seismic velocity toward the surface, a counteractive effect of damping, $D(f)$, applies at high frequencies (Anderson and Hough, 1984).

$$D(f) = exp^{(-\pi f \kappa_0)} \quad (15)$$

which κ_0 is a site-specific damping term related to Q. This exponential decay in high-frequency energy is proposed to primarily reflect source-station attenuation and local site response (Anderson & Hough, 1984; Ktenidou et al., 2013; Neighbors et al., 2015; Parolai, 2015).

A variety of approaches are proposed for estimating κ_0, the most commonly used is source spectra techniques (Ktenidou et al.,2014). Anderson and Hough, (1984) proposed an approach to estimate κ_0 using decay of the S-wave Fourier spectrum. In this study, κ_0 value obtained following spectral fitting method such that average path attenuation t^* can be given by $t^* = \kappa_0 + r_{hyp} /(Q\beta)$. The estimated κ_0 from this are study presented in Table 4.

Table 4 Estimated κ_0 from spectral fitting method

κ_0(s) from this study			**κ_0 (s) from Butcher et al. (2020)**	
Signal window	**Using all events**	**4 Biggest events only**	**Signal window**	
S-wave window	0.01	0.013	Noise window	0.027
Coda window	0.017	0.01	Coda window	0.03
S-coda window	0.007	0.002	Direct wave window	0.025

V. Final Remarks and Future Studies

This study has important consequences for understanding ground motions from induced earthquake at Preston New Road, and for future studies of seismic hazard from these typical events. Ground motion prediction equations (GMPEs) can be used to characterize peak amplitudes and response spectra as a function of magnitude, hypocentral distance, and other variables, for use in seismic hazard analysis (e.g. Atkinson, 2015; Yenier et al., 2017; Atkinson and Assatourians, 2017). Such GMPEs are not yet well-developed for induced events. Several studies have been carried out to develop GMPEs for induced seismicity (e.g. Atkinson, 2015), however, many of them still use the assumption that induced events have source and attenuation parameters that are broadly similar to those of natural earthquakes. Nevertheless, there is a significant systematic discrepancy in source properties between natural and induced earthquake. Induced earthquakes have systematically lower stress parameters than natural earthquakes (Hough, 2014). From the scaling relationships of Boore (1983) and Hanks and Johnston (1992), we know that high frequency ground motions depend strongly on the stress parameter and weakly on the moment magnitude.

The Preston New Road (PNR) dataset with magnitudes < 3 at distances less than 30 km was utilized in this study to better understand ground motion characteristics for induced seismicity and to work toward the development of a GMPE specifically designed for the magnitude and distance range of induced seismic events. Preliminary studies about GMPEs applied to data at PNR area has been conducted by Edwards et al. (2019) by simply borrowing GMPEs from Atkinson (2015) and Douglas et al. (2013) combined with magnitude model by Grünthal et al. (2009) and Edwards et al. (2015). Those approach in fact s not the best solution and still has limitations such as the unsatisfactory sigma. In order to avoid these limitations, we observe each different aspect (source, path, and site term) as tools for developing new GMPEs.

The work presented in this deliverable provides key elements required for the development of new GMPEs for PNR research area. Based on the study of attenuation parameters, in the case of induced earthquakes which occur at shallow depth, the seismic energy decayed more rapidly. This can be caused by physical properties that are quite different from the natural earthquakes. Hence, the use of GMPEs that directly adopted from natural or moderate-to-larger earthquakes does not represent the condition properly.

Further studies are underway to aid development of new GMPE specifically for induced earthquakes. In particular: the analysis of source parameters (how the depth as well as earthquake triggering mechanism could affect stress parameter); calibration and simulation based on physical properties in accordance with the characteristic of induced seismicity; and analysing the potential of regional differences in ground motion due to site effects by comparing with other regions.

Through a better understanding of ground motions and their controlling factors, future studies will be able to draw robust conclusions on the behaviour of ground motions from these events and reduce the uncertainty associated with GMPEs for induced events, such as those at Preston New Road.

References

Abercrombie, R. E., and P. Leary. (1993). Source Parameters of Small Earthquakes Recorded at 2.5 Km Depth, Cajon Pass, Southern California: Implications for Earthquake Scaling. Geophys. Res. Lett., 20(14), 1511–1514.

Anderson, J. G. and S. E. Hough. (1984). A model for the shape of the Fourier amplitude spectrum of acceleration at high frequencies. Bulletin of the Seismological Society of America, 74(5):1969-1993.

Atkinson, Gail M. (2015). Ground-motion prediction equation for small-to moderate events at short hypocentral distances, with application to induced seismicity hazards, *Bulletin of the Seismological Society of America* 105, doi: 10.1785/0120140142.

Atkinson, Gail M., and Karen Assatourians. (2017). Are Ground-Motion Models Derived from Natural Events Applicable to the Estimation of Expected Motions for Induced Earthquakes? *Seismological Research Letters*. 88, doi:10.1785/0220160153.

Aki, Keiiti & B. Chouet. (1975). Origin of Coda Waves: source, attenuation and scattering effects. Journal of Geophysical Research: Solid Earth. 80. 3322-3342. 10.1029/JB080i023p03322.

Ameri, G., C. Martin, and A. Oth (2020). Ground-Motion Attenuation, Stress Drop, and Directivity of Induced Events in the Groningen Gas Field by Spectral Inversion of Borehole Records, Bull. Seismol. Soc. Am. 110, 2077–2094, doi: 10.1785/0120200149

Bommer, Julian J., Bernard Dost, Benjamin Edwards, Pauline P.Kruiver, Michail Ntinalexis, Adrian Rodriguez-Marek, Peter J. Stafford and Jan Van Elk. (2017). Developing a model for the prediction of ground motions due to earthquakes in the Groningen gas field. *Netherlands Journal of Geosciences, 96*(5), S203-S213, doi:10.1017/njg.2017.28

Boore D. M. (1983). Stochastic simulation of high-frequency ground motions based on seismological models of the radiated spectra. Bull. Seismol. Soc. Am. 73, 1865–1894.

Boyd, O. S., D.E. McNamara, S.H. Hartzell, and G.L. Choy. (2017). Influence of Lithostatic Stress on Earthquake Stress Drops in North America. Bull. Seismol. Soc. Am., 107(2), 856–868.

Brune, J.N. (1970). Tectonic stress and the spectra of seismic shear waves from earthquakes. Journal of Geophysical Research, 75(26), pp.4997-5009.

Butcher, A., Richard Luckett, J.-Michael Kendall, Brian Baptie. (2020). Seismic Magnitudes, Corner Frequencies, and Microseismicity: Using Ambient Noise to Correct for High-Frequency Attenuation. *Bulletin of the Seismological Society of America:* 110 (3): 1260–1275, doi: 10.1785/0120190032

Castellaro, S., Francesco Mulargia, and Piermaria Rossi. (2008). Vs30: Proxy for Seismic Amplification?. Seismological Research Letters - SEISMOL RES LETT. 79. 540-543, doi:10.1785/gssrl.79.4.540.

Clarke, H., Leo Eisner, Peter Styles, and Peter Turner. (2014). Felt seismicity associated with shale gas hydraulic fracturing: The first documented example in Europe**.** Geophysical Research Letters, 41 (23) (2014), pp. 8308-8314.

Cuadrilla Resources. (2019b). Hydraulic Fracture Plan PNR 2, Technical Report CORP-HSERPT-003, 24 pp.

de Pater H. and Pellicer M. (2011). Geomechanical Study of Bowland Shale Seismicity – Fracture Geometry and Injection Mechanism, *StrataGen report for Cuadrilla.*

Deichmann, Nicholas. (2017). Theoretical Basis for the Observed Break in M_L / M_w Scaling between Small and Large Earthquakes. Bulletin of the Seismological Society of America. 107, doi: 10.1785/0120160318.

Dost, B., Benjamin Edwards. and Julian J. Bommer. (2018). The relationship between M and ML: a review and application to induced seismicity in the Groningen Gas Field, The Netherlands. Seismological Research Letters, 89(3), pp.1062-1074.

Douglas, J., and P. Jousset (2011). Modeling the difference in groundmotion magnitude-scaling in small and large earthquakes, Seismol. Res. Lett. 82, no. 4, 504–508, doi: 10.1785/gssrl.82.4.504.

Douglas, J., Benjamin Edwards., Vicenzo Convertito, Nitin Sharma, Anna Tramelli, Dirk Kraaijpoel, Bany Mena Cabrera, Nils Maercklin, and Claudia Troise. (2013). Predicting Ground Motion from Induced Earthquakes in Geothermal Areas. Bulletin of the Seismological Society of America. 103. 1875-1897, doi:10.1785/0120120197.

Douglas, J. and Benjamin Edwards. (2016). Recent and future developments in earthquake ground motion estimation. Earth-Science Reviews, 160, pp.203-219.

Douglas, J. (2019). Ground motion prediction equations 19642019, http://www.gmpe.org.uk.

Edwards, B. and John Douglas. (2013). Selecting ground-motion models developed for induced seismicity in geothermal areas. Geophysical Journal International, 195(2), pp.1314-1322.

Edwards, B., Andreas Rietbrock, Julian J. Bommer, and Brian Baptie. (2008). The acquisition of source, path, and site effects from microearthquake recordings using Q tomography: Application to the United Kingdom, Bull. Seismol. Soc. Am. 98, no. 4, 1915–1935.

Edwards, B., and Donat Fäh. (2013). A stochastic ground-motion model for Switzerland, Bull. Seismol. Soc. Am. 103, no. 1, doi: 10.1785/0120110331.

Edwards, B., Toni Kraft, Carlo Cauzzi, Philopp Kästli, and Stefan Wiemer. (2015). Seismic monitoring and analysis of deep geothermal projects in St Gallen and Basel, Switzerland. Geophysical Journal International, 201(2), pp.1022-1039.

Edwards, B., Helen Crowley, and Rui Pinho. (2019). Final Report on: "WP2-Impacts of Seismicity: Transmission to People, Propety and Well Integrity".

Edwards, B., Helen Crowley, and Rui Pinho. (2020). Final Report on: "WP2-Impacts of Seismicity: Transmission to People, Propety and Well Integrity".

Foulger, Gillian R., Miles P. Wilson, Jon G. Gulyas, Bruce R. Julian and Richard J. Davies. (2018). Global review of human-induced earthquakes. Earth-Science Reviews, volume 178, pages 438-514, ISSN 0012-8252. Doi: 10.1016/j.earscirev.2017.07.008.

Grünthal, G., Rutger Wahlström, and Dietrich Stromeyer. (2009). The unified catalogue of earthquakes in central, northern, and northwestern Europe (CENEC)—updated and expanded to the last millennium. Journal of Seismology, 13(4), pp.517-541.

Hanks T. C. (1979). *b* values and $\omega^{-\gamma}$ seismic source models: Implications for tectonic stress variations along active crustal fault zones and the estimation of high-frequency strong ground motion. J. Geophys. Res. 84, 2235–2242.

Hanks, T.C. and Hiroo Kanamori. (1979). A moment magnitude scale. Journal of Geophysical Research: Solid Earth, 84(B5), pp.2348-2350.

Hanks, T. C., and Arch C. Johnston. (1992). Common features of the excitation and propagation of strong ground motion for North American earthquakes, Bull. Seismol. Soc. Am.,82(1), 1– 23.

Hartzell, S., David Carver, Robert A. Williams, Stephen Harmsen, and Aspasia Zerva. (2001). Site response, shallow shear-wave velocity, and damage in Los Gatos, California, from the 1989 Loma Prieta earthquake. Bulletin of the Seismological Society of America 93, 443–464.

Hassani, B. and Gail M. Atkinson. (2016). Applicability of the site fundamental frequency as a Vs30 proxy for central and eastern North America. *Bulletin of the Seismological Society of America,*106(2),pp.653-664.

Hough S. E. (2014). Shaking from injection-induced earthquakes in the central and eastern United States. Bull. Seismol. Soc. Am. 104, 2619–2626.

Hough S. E. (2015). Shaking intensity from injection-induced versus tectonic earthquakes in the central-eastern United States. Leading Edge 34, 690–697.

Hough, S. E., and M. Page. (2015). A Century of Induced Earthquakes in Oklahoma? Bull. Seismol. Soc. Am., 105(6), 2863–2870.

Holmgren, J. M., G.M. Atkinson, and H. Ghofrani. (2019). Stress Drops and Directivity 104 of Induced Earthquakes in the Western Canada Sedimentary Basin. Bull. Seismol. Soc. Am., 109(5), 1635–1652.

Huang, Yihe, William L. Ellsworth, and Gregory C. Beroza. (2016). Stress Drop Estimates of Potentially Induced Earthquakes in the Guy-Greenbrier Sequence. J. Geophys. Res. Solid Earth, 121, 1–11.

Huang, Yihe, William L. Ellsworth, and Gregory C. Beroza. (2017). Stress drops of induced and tectonic earthquakes in the central United States are indistinguishable. Science Advances. 3. e1700772, doi: 10.1126/sciadv.1700772.

Kanamori, H. (1977). The Energy Release in Great Earthquakes. J. Geophys. Res., 82(20), 2981–2987.

Klose, C.. (2007). Coastal land loss and gain as potential earthquake trigger mechanism in SCRs. AGU Fall Meeting Abstracts. -1. 0759.

Ktenidou, O.-J., C. G´elis, and L.F. Bonilla. (2013). A study on the variabilityof kappa (κ) in a borehole: implications of the computation process,Bull.seism. Soc. Am.,103(2A), 1048–1068.

Luckett, R., Lars Ottemöller, Antony Butcher, and Brian Baptie. (2018). Extending local magnitude M_L to short distances. Geophys. J. Int. (2019) 216, 1145–1156, doi: 10.1093/gji/ggy484.

Neighbors, C., Javier Liao, Elizabeth Cochran, Gareth Funning, Angela Chung, Jesse Lawrence, Carl Christensen, Matthew Miller, A. Belmonte, and Héctor H. Sepúlveda. (2015). Investigation of the high-frequency attenuation parameter, (kappa), from aftershocks of the 2010 Mw 8.8 Maule, Chile earthquake. Geophysical Journal International. 200. 200-215. 10.1093/gji/ggu390.

Nievas, C.I., Julian J. Bommer, Helen Crowley, and Jan van Elk. (2020). Global occurrence and impact of small-to-medium magnitude earthquakes: a statistical analysis. Bull Earthquake Eng 18, 1–35, doi: 10.1007/s10518-019-00718-w

Novakovic M., and Gail M. Atkinson. (2015). Preliminary Evaluation of Ground Motions from Earthquakes in Alberta. Seismol. Res. Lett. 86(4), 1086-1095.

Novakovic M., Gail M. Atkinson, and Karen Assatourians. (2018). Empirically Calibrated Ground Motion Prediction Equation for Oklahoma. Bull. Seismol. Soc. Am, doi: 10.1785/0120170331.

Parolai, S., 2018. κ0: origin and usability, Bull. seism. Soc. Am., 108, 3446-3456

Perron, V., Aurore Laurendeau, Fabrice Hollender, Pierre-Yves Bard, Céline Gélis, Paola Traversa, and Stéphane Drouet. (2018). Selecting time windows of seismic phases and noise for engineering seismology applications: a versatile methodology and algorithm. *Bull Earthquake Eng* **16,** 2211–2225, doi:10.1007/s10518-017-0131-9.

Prieto, G.A., R.L. Parker, and F.L.Vernon III. (2009). A Fortran 90 library for multitaper spectrum analysis, Computers & Geosciences, 35, 1701–1710, doi: 10.1016/j.cageo.2008.06.007.

Rietbrock A, Fleur Strasser, and Benjamin Edwards. (2013). A stochastic earthquake ground-motion prediction model for the United Kingdom. Bulletin of the Seismological Society of America. 103,57–77, doi: 10.1785/0120110231.

Rietbrock, A. and Benjamin Edwards. (2019). Update of the UK stochastic ground motion model using a decade of broadband data. Proceedings of the SECED conference, 9-10th September 2019, Greenwich, London.

Ruhl, C. J., R.E. Abercrombie, and K.D. Smith. (2017). Spatiotemporal Variation of Stress Drop During the 2008 Mogul, Nevada, Earthquake Swarm. J. Geophys. Res. Solid Earth, 122(10), 8163–8180.

Sarker, G., G. Abers. (1998). Comparison of Sesimic Body Wave and Coda Wave Measures of Q. *Pure appl. geophys.* **153,** 665–683, doi:10.1007/s000240050213

Shearer, P.M. (2009). Introduction to Seismology,2nd Edition, Cambridge University Press, Cambridge.

Sargeant, S. and Lars Ottemöller. (2009). *Lg* wave attenuation in Britain. Geophysical Journal International, 179: 1593-1606, doi:10.1111/j.1365-246X.2009.04325.x

Stewart, Jonathan P., John Douglas, Mohammad Javanbarg, Yousef Bozorgnia, Norman A. Abrahamson, David M. Boore, Kenneth W. Campbell, Elise Delavaud, Mustafa Erdik, and Peter J. Stafford. (2015). Selection of ground motion prediction equations for the global earthquake model. Earthq Spectra 31(1):19–45, doi:10.1193/013013EQS017

Theodulidis N, and Pierre-Yves Bard. (1995). Horizontal to vertical spectral ratio and geological conditions: an analysis of strong motion data from Greece and Taiwan. Soil Dyn Earthqu Eng 14:177–197

Wilson, M., Richards J. Davies, Gillian Foulger, and B.R. Julian. (2015). Anthropogenic earthquakes in the UK: A national baseline prior to shale exploitation, Marine and Petroleum Geology, doi:10.1016/j.marpetgeo.2015.08.023.

Yenier, E. (2017). A Local Magnitude Relation for Earthquakes in the Western Canada Sedimentary Basin. Bull. Seismol. Soc. Am. 107. 10.1785/0120160275.

Yenier, E., and Gail M.Atkinson. (2015). An equivalent point-source model for stochastic simulation of earthquake ground motions in California. Bull. Seismol. Soc. Am.105, 1435-1455, doi: 10.1785/0120140254.

Yenier, E., and Gail M.Atkinson. (2014). Equivalent point-source modelling of moderate-to-large magnitude earthquakes and associated ground motion saturation effects, Bull. Seismol. Soc. Am.104, 1458-1478.

Zhang, H., D. W. Eaton, G. Li, Y. Liu, and R.M. Harrington. (2016). Discriminating Induced Seismicity from Natural Earthquakes Using Moment Tensors and Source Spectra. J. Geophys. Res. Solid Earth, 121, 972–993.